MANCHESTER 1824
The University of Manchester

The University of Manchester Research

# Upscaling non-Newtonian rheological fluid properties from pore-scale to Darcy's scale

**DOI:**
10.1016/j.ces.2021.116638

**Document Version**
Accepted author manuscript

Link to publication record in Manchester Research Explorer

**Citation for published version (APA):**
Shende, T., Niasar, V., & Babaei, M. (2021). Upscaling non-Newtonian rheological fluid properties from pore-scale to Darcy's scale. *Chemical Engineering Science*, *239*(116638), Article 116638. https://doi.org/10.1016/j.ces.2021.116638

**Published in:**
Chemical Engineering Science

**Citing this paper**
Please note that where the full-text provided on Manchester Research Explorer is the Author Accepted Manuscript or Proof version this may differ from the final Published version. If citing, it is advised that you check and use the publisher's definitive version.

**General rights**
Copyright and moral rights for the publications made accessible in the Research Explorer are retained by the authors and/or other copyright owners and it is a condition of accessing publications that users recognise and abide by the legal requirements associated with these rights.

**Takedown policy**
If you believe that this document breaches copyright please refer to the University of Manchester's Takedown Procedures [http://man.ac.uk/04Y6Bo] or contact openresearch@manchester.ac.uk providing relevant details, so we can investigate your claim.

OPEN ACCESS

Download date:13. May. 2025

# Upscaling non-Newtonian rheological fluid properties from pore-scale to Darcy's scale

Takshak Shende[a], Vahid Niasar[a], Masoud Babaei[a,*]

[a] *Department of Chemical Engineering and Analytical Science, The University of Manchester, Manchester, UK*

**Abstract**

Continuity and momentum equations govern the pore-scale flow properties of the fluid in the porous media, whereas Darcy's law governs Darcy scale properties of the fluid transport in porous media. The empirical shift factor relates the steady shear-dependent viscosity of non-Newtonian fluids to the Darcy viscosity in porous media. The reported values of the empirical shift factor cover three orders of magnitude depending on the considered fluid-medium configurations. This creates a challenge to upscale non-Newtonian rheology from pore-scale to Darcy's scale. We upscale Darcy viscosity based on pore-scale shear viscosity of Meter model fluid and viscoelastic linear Phan-Thien-Tanner fluid. We propose a Bundle-of-Capillaries model modified with pore-correction coefficient and fluid-correction coefficient. We numerically simulate the flow of polyacrylamide fluid, modelled using Meter model and linear Phan-Thien-Tanner model, through 3D symmetric micro-channel, 2D porous medium and 3D Mt Simon sandstone. Pore-scale direct numerical simulation using linear Phan-Thien-Tanner model showed viscoelastic instability in heterogeneous Mt Simon sandstone at low Reynolds number flow. Direct numerical simula-

*Corresponding author
*Email address:* masoud.babaei@manchester.ac.uk (Masoud Babaei)

tions overestimate Darcy viscosity due to the presence of stagnant zones without active flow.

*keywords*: Upscaling, Non-Newtonian fluids, Polymeric fluids, Bundle-of-Capillaries model, Direct numerical simulation

---

## 1. Introduction

Polymeric fluid flow in porous medium is of significant importance in many engineering applications such as enhanced oil recovery. Most of the polymeric solutions employed for the enhanced oil recovery applications show non-Newtonian behaviour [1, 2, 3, 4]. The commonly used non-Newtonian fluids (i.e. xanthan gum [5, 6] and polyacrylamide solution [7, 8]) for oil recovery show viscoelastic properties. The rheology of non-Newtonian fluids can be studied considering non-Newtonian fluid as a generalised Newtonian fluid (*e.g.* power-law, Bingham, Cross, Carreau, Elis, Meter model etc.) or viscoelastic fluid (*e.g.* Maxwell, Oldroyd-B, Giesekus, Phan–Thien—Tanner model etc.) [9, 10]. These models are derived based on an empirical approach with many simplified assumptions; thus, each model has its own limitations and cannot universally be applied to all types of non-Newtonian fluids [10].

The flow of polymeric solution in rheometer is remarkably different from that of the flow in porous medium. The reason could be [11] (i) the porous medium has complex geometry compared to rheometers; (ii) the presence of many expansion and contraction in the porous medium expose polymer to the various amount of shear stress [3]; (iii) mechanical retention and adsorption of the polymer change the geometry of the porous medium. To describe polymeric fluid behaviour in porous medium, apparent viscosity or Darcy viscosity is a commonly used terms in the literature [11, 3, 12, 13, 14]. Darcy viscosity ($\eta_{\text{darcy}}$) is defined using Darcy's law as [2, 1, 15],

$$\eta_{\text{darcy}} = \frac{Ak}{Q}\frac{dP}{dx} = \frac{k}{U_{\text{darcy}}}\frac{dP}{dx} \tag{1}$$

here, $A$ [m$^2$] is the cross-section area of the porous medium, $k$ [m$^2$] is the intrinsic permeability, $Q$ [m$^3$/s] is the volumetric flow rate, and $U_{\text{darcy}}$

[m/s] is the Darcy velocity, $\frac{dP}{dx}$ [Pa/m] is the pressure gradient. The Darcy viscosity is generally measured by performing core flood experiments [3]. Darcy viscosity of the polymeric fluid in porous medium depends on non-Newtonian rheology (measured using rheometer), inaccessible pore volume, degradation of the polymer due to mechanical or chemical forces, adsorption of polymer on pore surface, elastic stretching of polymeric molecules [16, 7]. Thus, the values of shear viscosity and Darcy viscosity for same non-Newtonian fluid show shift in the viscosity profile [17, 12, 2, 13, 18].

### *1.1. The shift factor*

The analytical solution of fluid flow in a circular capillary for the power-law model ($\eta = m\,\dot{\gamma}^n$) is used in bundle of capillary model along with the Blake-Kozeny equation to determine hydraulic radius ($R_\mathrm{h}$), Darcy viscosity ($\eta_\mathrm{darcy}$), and Darcy shear rate ($\dot{\gamma}_\mathrm{darcy}$) of the porous medium as [19],

$$R_\mathrm{h} = \sqrt{\frac{8k\psi}{\phi}} \tag{2}$$

$$\eta_\mathrm{darcy} = \left(\frac{3n+1}{4n}\right)^{\frac{1}{n-1}} \left(\frac{R_\mathrm{h}}{2\,m}\frac{dP}{dx}\right)^{1/n} \tag{3}$$

$$\dot{\gamma}_\mathrm{darcy} = 4\left(\frac{3n+1}{4n}\right)^{\frac{1}{n-1}} \left(\frac{U_\mathrm{darcy}}{\sqrt{8\,k\,\psi\,\phi}}\right) \tag{4}$$

here, $\eta$ [Pa·s] is the shear viscosity, $\dot{\gamma}$ [$\mathrm{s}^{-1}$] is the shear rate, $\psi$ is the tortuosity, $\phi$ is the porosity, $m$ and $n$ are model parameters of power-law fluid. The correlation between Darcy shear rate and Darcy velocity is defined using shift factor ($\alpha$) as [12, 2, 13, 15, 20],

$$\dot{\gamma}_\mathrm{darcy} = \alpha\,\frac{U_\mathrm{darcy}}{\sqrt{k\,\phi}} \tag{5}$$

here, $\sqrt{k\,\phi}$ is the microscopic characteristic pore length [2]. The empirical shift factors are introduced in the definition of the porous medium's shear rate in order to fit the Darcy viscosity ($\eta_{\text{darcy}}$) to the shear viscosity ($\eta$) [21].

Balhoff and Thompson [22] developed a macroscopic model to study the effect of fluid rheology and bed morphology on the flow of Ellis model fluids based on a pore-network model. Berg and Wunnik [12] carried out pore-scale simulation in sandstone rock and pointed out the shortcoming of Cannella or Blake–Kozeny equation for correlating shear rate with the Darcy viscosity using empirical shift factor ($\alpha$). Zami-Pierre *et al.* [23] studied the effect of the depletion layer at pore-boundary on quantification of the Darcy viscosity. Pore network modelling has been used to study the effect of shift factor on in-situ rheology in the porous medium [24, 17].

Rodríguez de Castro and Agnaou [13] numerically studied the effect of shear rheology model (power-law, Carreau model and Herschel-Bulkley model), pore size distribution, and geometrical variability on Darcy shear rate and Darcy velocity in the porous medium. Rodrıguez de Castro and Radilla [15] proposed a framework to relate the shear viscosity of Carreau model fluids with the Darcy viscosity in fractured porous medium. But, the authors neglected low-shear-viscosity plateau of Carreau model in the formulations for Darcy viscosity, given that only moderate and high shear rates were involved in their experiments. Zhang *et al.* proposed a correlation for $\alpha$ for the flow of the Cross model fluid in a rough fracture and showed that $\alpha$ depends on geometric tortuosity [21]. Zamani *et al.* [25] showed that $\alpha$ is a function of the porous medium properties (*i.e.* coordination number, tortuosity, aspect ratio) and rheology of the fluid. The significance of the shift factor is established for non-Newtonian fluid flow in the porous medium [3, 12, 13, 15, 19, 21, 23, 26, 27]. We note that the

values of $\alpha$ vary three orders of magnitude in literature [12, 13, 19].

The oversimplified approach to estimate the shear rate (*e.g.* avoiding pore-size distribution and effect of non-circular cross-sections [25]) and neglecting heterogeneity of porous medium in these models make the estimation of Darcy viscosity and Darcy shear rate of non-Newtonian fluids inconsistent.

Majority of the fluids in porous medium flow at low shear values. The power-law model fails to describe Newtonian behaviour (*i.e.* constant viscosity plateau) of polymeric solution at low-shear values. Ellis model gives extremely low viscosity values at high shear rate [28, 29]. Carreau [1], Carreau-Yasuda [30], Cross [31], Meter [32] models correctly depicts S-shape type shear thinning behaviour (*i.e.* Newtonian plateau at low as well as high shear values and decreasing viscosity at an intermediate shear values) of many polymeric solutions [15, 17]. Thus, equations to determine macroscopic (i.e. upscaled) Darcy viscosity, Darcy shear rate, Darcy shear stress using measurable parameters and without the shift factor ($\alpha$) are needed for the flow of a generalised Newtonian fluid and viscoelastic fluid in porous medium.

The flow of polymeric fluids through simple geometry (such as periodic array of cylinders, disorder porous medium) is previously studied by numerically simulating generalised Newtonian fluid (i.e power-law, Carreau, Cross model etc.) and viscoelastic fluid (i.e. FENE, PTT, Oldroyd-B etc.) [14, 33, 34, 35, 23, 36, 37, 38, 39, 40, 4, 41, 42, 43, 44, 45, 46, 47, 48, 49, 8, 50, 51]. The experiments as well as numerical results have shown viscoelastic instability at low Reynolds number for non-Newtonian fluid flows in porous media [51, 16, 52, 13, 53, 7, 54, 55, 56, 57, 58, 59]. However, numerical simulation studies of Meter model fluid (GNF) and Phan–Thien—Tanner model fluid (viscoelastic) flow through a heterogeneous porous medium such

as sandstone is absent in the literature.

### *1.2. Present study*

To address the above discrepancies, we propose a tortuous Bundle-of-Capillaries model for the flow of non-Newtonian fluids described by Meter model and Phan–Thien—Tanner model in Section 3. The proposed Bundle-of-Capillaries model (hereafter referred to as BCM) for non-Newtonian fluids takes into account the geometric variability of the porous medium, the pore-size distribution, and the S-shape type rheological behaviour (using Meter model) and viscoelastic behaviour (using linear Phan–Thien—Tanner model) of the non-Newtonian fluids. We derive upscaled Darcy viscosity, effective Darcy shear rate, effective Darcy shear stress, effective Reynolds number and effective Péclet number from pore-scale shear viscosity. We validate the proposed method using experimental data from the literature and pore-scale direct numerical simulations in Section 5.2 and 5.3, respectively. We also numerically simulate the flow of shear stress-dependent Meter model fluids and viscoelastic linear Phan–Thien—Tanner (PTT) model fluids in heterogeneous porous medium using OpenFOAM and validate the numerical simulation approach using experimental microfluidic observations in Section 5.3.1. Section 5.3.2 compares results obtained by direct numerical simulation with BCM approach and shows that the BCM captures the contribution of viscosity in the active flow of the polymeric fluid in the pore-space of porous medium.

## 2. Mathematical formulation

### *2.1. Governing equations*

The continuity equation (Eq. 6), momentum equation (Eq. 7) and constitutive equation of fluids describe single-phase, incompressible, laminar

flow of non-Newtonian fluids through void space [1].

$$\nabla \cdot \mathbf{u} = 0 \tag{6}$$

$$\rho \left( \frac{\partial \mathbf{u}}{\partial t} + \mathbf{u} \cdot \nabla \mathbf{u} \right) = -\nabla P + \nabla \cdot \boldsymbol{\tau} \tag{7}$$

here, $P$ [Pa] is the pressure, $t$ [s] is the time, $\mathbf{u}$ is velocity vector, and $\boldsymbol{\tau}$ is the stress tensor. The constitutive equation of the stress tensor of non-Newtonian fluid can be defined considering polymeric fluid as a generalised Newtonian fluid (*i.e* power-law, Bingham, Cross, Carreau, Meter model etc.) or viscoelastic fluid (*i.e.* Oldroyd-B, Giesekus, FENE, PTT etc.) [1, 9]. We note that these constitutive equations of non-Newtonian fluids have been developed based on empirical approach with simplified assumptions, thus, they have their own limitations [60, 10]. The Meter model (generalised Newtonian fluid) [32] and linear Phan-Thien–Tanner model (viscoelastic fluid) [61] have analytical solutions for laminar flow through circular geometry [62, 63]. We used above model in present work as analytical solutions [62, 63] helped us develop bundle of capillary model for non-Newtonian fluid as described in section 3.

#### *2.1.1. Meter model*

The constitutive equation of a shear stress-dependent generalised Newtonian fluid is [32, 28, 63]

$$\boldsymbol{\tau} = 2\,\eta(\tau)\,\mathbf{D} = \eta(\tau)\,(\nabla \mathbf{u} + (\nabla \mathbf{u})^T) \tag{8}$$

Where $\eta(\tau)$ is the shear viscosity of the fluid, which is a function of shear stress. The magnitude of the rate of strain tensor and stress tensor

for shear-dominated flow is as follows [32, 28, 60]

$$\dot{\gamma} = \sqrt{\frac{\dot{\boldsymbol{\gamma}} : \dot{\boldsymbol{\gamma}}}{2}} = \sqrt{2\mathbf{D} : \mathbf{D}} \tag{9}$$

$$\tau = \sqrt{\frac{\boldsymbol{\tau} : \boldsymbol{\tau}}{2}} = \sqrt{\frac{\eta\dot{\boldsymbol{\gamma}} : \eta\dot{\boldsymbol{\gamma}}}{2}} = \eta\sqrt{\frac{(\dot{\boldsymbol{\gamma}} : \dot{\boldsymbol{\gamma}})}{2}} = \eta\sqrt{(2\mathbf{D} : \mathbf{D})} \tag{10}$$

here, $\dot{\boldsymbol{\gamma}} = (\nabla\mathbf{u} + (\nabla\mathbf{u})^T)$ and $\mathbf{D} = \frac{1}{2}\dot{\boldsymbol{\gamma}}$

We define S-shape type non-Newtonian rheology of the polymeric solution using shear stress-dependent Meter model (Eq. 11) [32, 63],

$$\eta = \eta_\infty + \frac{\eta_0 - \eta_\infty}{1 + \left(\frac{\tau}{\tau_m}\right)^S} \tag{11}$$

where, $\eta$ [Pa·s] is the shear viscosity at a given shear stress ($\tau$); $\eta_0$ [Pa·s] is the zero shear viscosity; $\eta_\infty$ [Pa·s] is an infinite shear viscosity; $\tau_m$ [Pa] is a shear stress of the non-Newtonian fluid at which viscosity of the solution drops to $\frac{\eta_0+\eta_\infty}{2}$; $S$ is the shear stress-dependent exponent of Meter model which represent the slope of shear thinning or shear thickening fluid. The characteristic time $\lambda$ [s] of Meter model fluid is $\lambda = \frac{\eta_0+\eta_\infty}{2\,\tau_m}$. If $\eta_0 = \eta_\infty$, Meter model converts to Newtonian fluid. Meter model represents a shear thinning fluid (if $\eta_0 > \eta_\infty$), and shear thickening fluid (if $\eta_0 < \eta_\infty$). The analytical solution for radial velocity profile ($u(r)$) and average velocity ($U$) of a fluid flow obeying Meter model equation in a circular geometry of radius ($R$) at pressure gradient of $\frac{dP}{dx}$ are as given in Eq. 12 and 13, respectively [63].

$$u(r) = -\frac{dP}{dx}\frac{1}{4\,\eta_0\,\eta_\infty}\Bigg[R^2\left(\eta_0 + (\eta_\infty - \eta_0)\,{}_2\mathrm{F}_1\left(1, \frac{2}{S}; \frac{S+2}{S}; -\frac{\eta_\infty}{\eta_0}\left(-\frac{dP}{dx}\frac{R}{2\,\tau_\mathrm{m}}\right)^S\right)\right) - r^2\left(\eta_0 + (\eta_\infty - \eta_0)\,{}_2\mathrm{F}_1\left(1, \frac{2}{S}; \frac{S+2}{S}; -\frac{\eta_\infty}{\eta_0}\left(-\frac{dP}{dx}\frac{r}{2\,\tau_\mathrm{m}}\right)^S\right)\right)\Bigg], \tag{12}$$

$$U = -\frac{dP}{dx}\frac{R^2}{8\,\eta_\mathrm{eff}} \tag{13}$$

Here, $\eta_\mathrm{eff}$ (Eq 14) is the effective viscosity of the fluid for a given set of fluid flow condition [63].

$$\frac{1}{\eta_\mathrm{eff}} = \frac{1}{\eta_0\,\eta_\infty}\Bigg((\eta_\infty - \eta_0)\,{}_3\mathrm{F}_2\left(1, \frac{2}{S}, \frac{4}{S}; \frac{S+2}{S}, \frac{S+4}{S}; -\frac{\eta_\infty}{\eta_0}\left(-\frac{dP}{dx}\frac{r}{2\,\tau_\mathrm{m}}\right)^S\right) + 2\,(\eta_0 - \eta_\infty)\,{}_2\mathrm{F}_1\left(1, \frac{2}{S}; \frac{S+2}{S}; -\frac{\eta_\infty}{\eta_0}\left(-\frac{dP}{dx}\frac{r}{2\,\tau_\mathrm{m}}\right)^S\right) - \eta_0\Bigg), \tag{14}$$

where, ${}_2F_1(a, b; c; z)$ and ${}_3F_2(a, b, c; d, e; z)$ are the hypergeometric function. The `hypergeom` function of MATLAB can be utilised to solve hypergeometric function, which is computationally expensive. Thus, Shende *et al.,* [63] proposed computationally inexpensive Eq. 15 to determine the approximate effective viscosity of the Meter model fluid flow.

$$\eta_\mathrm{eff} = \eta_\infty + \frac{\eta_0 - \eta_\infty}{1 + \left(\dfrac{0.8\,R}{2\,\tau_\mathrm{m}}\dfrac{dP}{dx}\right)^S} \tag{15}$$

Shende *et al.* [63] have shown that effective viscosity helps to estimate the Reynolds number of non-Newtonian fluid through circular geometry correctly.

*2.1.2. Linear Phan-Thien and Tanner (PTT) model*

The constitutive equations of the affine version of linear PTT viscoelastic model proposed by Phan-Thien and Tanner are [61, 62, 64, 51, 65]

$$f(\mathrm{tr}(\boldsymbol{\tau}))\cdot\boldsymbol{\tau}+\lambda\left(\frac{\partial\boldsymbol{\tau}}{\partial t}+\mathbf{u}\cdot\boldsymbol{\nabla}\boldsymbol{\tau}-\boldsymbol{\tau}\cdot\nabla\mathbf{u}-(\nabla\mathbf{u})^{T}\cdot\boldsymbol{\tau}\right)=\eta_{\mathrm{p}}(\nabla\mathbf{u}+(\nabla\mathbf{u})^{T}) \tag{16}$$

here, $\lambda$ is the relaxation time, $\eta_{\mathrm{p}}$ is the polymeric fluid contribution to the zero shear viscosity ($\eta_0$). Here, $\eta_0=\eta_{\mathrm{p}}+\eta_{\mathrm{s}}$ and $\eta_{\mathrm{s}}$ is the solvent viscosity [65]. $\boldsymbol{\tau}$ is the polymeric extra-stress tensor. The stress invariants function $f(\mathrm{tr}(\boldsymbol{\tau}))$ in above equation for PTT follows linear form as given in Eq. 17 [61, 62],

$$f(\mathrm{tr}(\boldsymbol{\tau}))=\left[1+\frac{\varepsilon\,\lambda}{\eta_{\mathrm{p}}}\mathrm{tr}(\boldsymbol{\tau})\right] \tag{17}$$

The constant parameter $\varepsilon$ ($0\leq\varepsilon\leq 1$) represents the extensional properties [65] of the viscoelastic fluid.

Oliveira and Pinho [62] derived an exact analytical solution for radial velocity profile (Eq. 18) and average velocity (Eq. 19) for linear PTT model fluid flow through circular pipe.

$$u(r)=-\frac{dP}{dx}\,\frac{\left(R^2-r^2\right)}{4\,\eta_{\mathrm{p}}}\left(1+\frac{\varepsilon\,\lambda^2\left(\dfrac{dP}{dx}\right)^2}{4\,\eta_{\mathrm{p}}^2}\left(R^2+r^2\right)\right) \tag{18}$$

$$U = -\frac{dP}{dx}\,\frac{R^2}{8\,\eta_{\rm p}}\left(1+\frac{\varepsilon\,\lambda^2\,R^2\,\left(\dfrac{dP}{dx}\right)^2}{3\,\eta_p^2}\right) \tag{19}$$

Similar to the approach adopted by [63, 66], on equating Eq. 19 with Hagen–Poiseuille equation, we obtain the effective viscosity ($\eta_{\rm eff}$) of linear PTT fluid flow as,

$$\frac{1}{\eta_{\rm eff}} = \frac{1}{\eta_{\rm p}}\left(1+\frac{\varepsilon\,\lambda^2\,R^2\,\left(\frac{dP}{dx}\right)^2}{3\,\eta_p^2}\right) \tag{20}$$

## 3. Bundle-of-Capillaries model (BCM) for non-Newtonian fluids

We assume that $N$ number of tortuous capillaries of varying radii and length L are kept in parallel in a porous medium of size ($d \times d \times L$), here, cross-sectional area of the medium is $A = d^2$ . The bundle of circular capillaries consists of a set of different radii and each radius ($r_i$) appearing $N_i$ times in a porous medium. The relative frequency ($n_i$) of a radius ($r_i$) in a bundle of capillaries is $n_i = \frac{N_i}{\sum N_i}$ and $\sum n_i = 1$. Thus, porosity ($\phi$) of the porous medium will be,

$$\phi = \frac{V_v}{V} = \frac{\sum n_i\,\pi\,r_i^2}{d^2}, \tag{21}$$

where, $V_v$ is the volume of voids, and $V$ is the total volume. We note that due to the heterogeneous nature, pore-size distribution of the porous medium cannot always be defined using single probability density function (*e.g.* log-normal distribution, Weibull distribution etc.). Thus, we have not defined pore-size distribution using any functional form.

### *3.1. Pore-correction coefficient ($\beta_p$)*

We note that the micro-capillaries in the porous medium follow tortuous paths [14] and the non-circular cross-sectional area of a single micro-capillary varies along its path. To account for this variation, we define hydraulic radius ($r_{\mathrm{h,N}}$) of a single micro-capillary during the flow of Newtonian fluid as $r_{\mathrm{h,N}} = \beta_{\mathrm{p}}\, r$, where, $\beta_{\mathrm{p}}$ is the pore-correction coefficient of a micro-capillary and $r$ [m] is the inscribed pore radius. Adopting Hagen–Poiseuille equation, we define average pore velocity ($U_{\mathrm{N}}$) of a Newtonian fluid in a bundle of micro-capillaries in parallel as,

$$U_{\mathrm{N}} = \sum n_i\, u_i = \frac{1}{8\,\mu}\,\frac{dP}{dx}\,\sum n_i\,(\beta_{\mathrm{p}}\, r_i)^2, \tag{22}$$

here, $u_i$ [m/s] is the average velocity of fluid in a micro-capillary of radius $r_i$, and $\mu$ [Pa·s] is the Newtonian viscosity. The tortuosity ($\psi$) of the porous medium is $\psi = \frac{L_g}{L_s}$, where, $L_g$ is the average flow path of porous medium and $L_s$ is the straight line length [67]. Thus, average velocity of Newtonian fluid (*i.e.* Darcy velocity) in the porous medium will be,

$$U_{\mathrm{N,D}} = \phi\,\frac{U_{\mathrm{N}}}{\psi} = \frac{\phi}{8\,\mu\,\psi}\,\frac{dP}{dx}\,\sum n_i\,(\beta_{\mathrm{p}}\, r_i)^2, \tag{23}$$

Equating Eq. 23 with Darcy's law ($U_{\mathrm{N,D}} = \frac{k}{\mu}\,\frac{dP}{dx}$) gives the intrinsic permeability ($k$) as,

$$k = \frac{\phi}{8\,\psi}\,\sum n_i\,(\beta_{\mathrm{p}}\, r_i)^2 \tag{24}$$

Eq. 24 suggests that $\beta_p$ of the porous medium can be determined using measurable parameters (*i.e.* permeability ($k$), porosity ($\phi$), and the pore-size distribution). We note that in the parallel bundle of micro-capillaries, flow through large pore dominates [68, 69]. On the contrary, in reality, the small pores in porous medium control the total flow. The pore-correction

coefficient ($\beta_p$), which is an averaging parameter of the pore radius, helps balance this variation.

### *3.2. Fluid-correction coefficient ($\beta_f$)*

Many non-Newtonian fluids used in industry are polymer solutions. Thus, they are susceptible to adsorption, pore-clogging and deposition in the pore spaces [23]. Adsorption of polymer on the surface of a micro-capillary alters the pore-geometry of the micro-capillary. Also, the elastic properties of non-Newtonian fluids stretch or contract polymeric molecules in the pore space [70, 7]. This creates additional resistance to the non-Newtonian fluid flow through tortuous micro-capillaries. Thus, we define hydraulic radius of micro-capillary for flow of non-Newtonian fluids as $r_{\mathrm{h,NN}} = \beta_{\mathrm{f}}\, r_{\mathrm{h,N}} = \beta_{\mathrm{f}}\, \beta_{\mathrm{p}}\, r$, where, $\beta_{\mathrm{f}}$ is the fluid-correction coefficient of micro-capillary due to fluid rheology during non-Newtonian fluid flow.

The analytical solution for average velocity ($u_{\mathrm{NN}}$) of a non-Newtonian fluid in a micro-capillary of the hydraulic radius ($r_{\mathrm{h,\ NN}}$) is,

$$u_{\mathrm{NN}} = \frac{(\beta_{\mathrm{f}}\, \beta_{\mathrm{p}}\, r)^2}{8\, \eta_{\mathrm{eff}}}\, \frac{dP}{dx}, \tag{25}$$

here, $\eta_{\mathrm{eff}}$ for Meter model fluid will be as in Eq 26 and $\eta_{\mathrm{eff}}$ for linear PTT viscoelastic model fluid will be as in Eq. 27,

$$\eta_{\mathrm{eff}} = \eta_{\infty} + \frac{\eta_0 - \eta_{\infty}}{1 + \left(\dfrac{0.8\, (\beta_{\mathrm{f}}\, \beta_{\mathrm{p}}\, r)}{2\, \tau_m}\, \dfrac{dP}{dx}\right)^S} \tag{26}$$

$$\frac{1}{\eta_{\mathrm{eff}}} = \frac{1}{\eta_{\mathrm{p}}} \left(1 + \frac{\varepsilon\, \lambda^2\, (\beta_{\mathrm{f}}\, \beta_{\mathrm{p}}\, r)^2\, \left(\frac{dP}{dx}\right)^2}{3\, \eta_p^2}\right) \tag{27}$$

Note that $\eta_{\mathrm{eff}}$ is a function of the radius of micro-capillary, thus, an average pore velocity of non-Newtonian fluids ($U_{\mathrm{NN}}$) in a bundle of parallel

capillaries is,

$$U_{\mathrm{NN}} = \frac{1}{8}\,\frac{dP}{dx}\,\sum \frac{n_i\,(\beta_{\mathrm{f}}\,\beta_{\mathrm{p}}\,r_i)^2}{\eta_{\mathrm{eff,i}}}, \tag{28}$$

The average velocity (*i.e.* Darcy velocity) of non-Newtonian fluids in a tortuous porous medium will be,

$$U_{\mathrm{NN,D}} = \phi\,\frac{U_{\mathrm{NN}}}{\psi} = \frac{\phi}{8\,\psi}\,\frac{dP}{dx}\,\sum \frac{n_i\,(\beta_{\mathrm{f}}\,\beta_{\mathrm{p}}\,r_i)^2}{\eta_{\mathrm{eff,i}}}, \tag{29}$$

On equating Eq. 1 with Eq. 29, we get hydraulic conductivity or conductance ($K$) of porous medium as,

$$K = \frac{k}{\eta_{\mathrm{darcy}}} = \frac{\phi}{8\,\psi}\,\sum \frac{n_i\,(\beta_{\mathrm{f}}\,\beta_{\mathrm{p}}\,r_i)^2}{\eta_{\mathrm{eff,i}}} \tag{30}$$

Substituting Eq. 24 in Eq. 30, we obtain the non-Newtonian fluid's upscaled Darcy viscosity as follow,

$$\eta_{\mathrm{darcy}} = \frac{\sum n_i\,(\beta_{\mathrm{p}}\,r_i)^2}{\sum \frac{n_i\,(\beta_{\mathrm{f}}\,\beta_{\mathrm{p}}\,r_i)^2}{\eta_{\mathrm{eff,i}}}} \tag{31}$$

The volumetric flow rate ($Q_{\mathrm{NN,D}}$) of the non-Newtonian fluid in a porous medium is,

$$Q_{\mathrm{NN,D}} = d^2\,U_{\mathrm{NN,D}} = \frac{d^2\,\phi}{8\,\psi}\,\frac{dP}{dx}\,\sum \frac{n_i\,(\beta_{\mathrm{f}}\,\beta_{\mathrm{p}}\,r_i)^2}{\eta_{\mathrm{eff,i}}}, \tag{32}$$

We obtain the volumetric flow rate of the non-Newtonian fluid in terms of the pore radius by substituting Eq. 21 in Eq. 32

$$Q_{\mathrm{NN,D}} = \frac{1}{8\,\psi}\,\frac{dP}{dx}\,\sum \frac{n_i\,(\beta_{\mathrm{f}}\,\beta_{\mathrm{p}}\,r_i)^2}{\eta_{\mathrm{eff,i}}}\,\sum n_i\,\pi\,r_i^2 \tag{33}$$

Eq. 29 and Eq 33 suggest that the $\beta_{\mathrm{f}}$ can be determined using measurable parameters (*i.e.* Darcy's flow rate/velocity, pore-size distribution, porosity ($\phi$), tortuosity, and model parameters of non-Newtonian fluid.)

### *3.3. Effective (upscaled) parameters*

Effective viscosity of the fluid is the representative viscosity (*i.e.* upscaled viscosity) for a given set of flow conditions in a circular capillary [63]. Similarly, effective shear rate and effective shear stress are representative values (i.e. upscaled Darcy values) for a given set of flow conditions in porous medium, which take into account pore-size distribution and pore-scale variability. We define the effective shear stress ($\tau_{\text{eff}}$) in the porous medium during the non-Newtonian fluid flow as,

$$\tau_{\text{eff}} = \sum n_i \, \tau_i = \frac{1}{2} \frac{dP}{dx} \sum n_i \, (\beta_{\text{f}} \, \beta_{\text{p}} \, r_i), \tag{34}$$

Here, $\tau_i$ is the wall shear stress in the micro-capillary of radius $r_i$. Similarly, the effective shear rate ($\dot{\gamma}_{\text{eff}}$) in the porous medium is defined as in Eq. 35,

$$\dot{\gamma}_{\text{eff}} = \sum n_i \, \frac{\tau_i}{\eta_{\text{eff,i}}} = \frac{1}{2} \frac{dP}{dx} \sum \frac{n_i \, (\beta_{\text{f}} \, \beta_{\text{p}} \, r_i)}{\eta_{\text{eff,i}}} \tag{35}$$

Reynolds number of the porous medium is generally defined using particle diameter [71, 2]. It is highly unlikely to correctly define particle diameter of the porous medium such as rocks. Furthermore, Reynolds number of fluid flow in porous medium is a pore-scale property which must be defined using geometry of the pore-space. Thus, adopting Shende *et al.* [63] approach, we define the effective Reynolds number ($Re_{\text{eff}}$) and the effective Péclet number ($Pe_{\text{eff}}$) of a fluid flow in porous medium as in Eq. 36 and Eq. 37, respectively,

$$Re_{\text{eff}} = \sum n_i \, Re_i = 2 \, \rho \sum \frac{n_i \, u_i \, (\beta_{\text{f}} \, \beta_{\text{p}} \, r_i)}{\psi \, \eta_{\text{eff,i}}} \tag{36}$$

$$Pe_{\text{eff}} = \sum n_i \, Pe_i = \sum \frac{n_i \, u_i \, (\beta_{\text{f}} \, \beta_{\text{p}} \, r_i)}{\psi \, D_{\text{m}}} \tag{37}$$

Here, $Re_i$ and $Pe_i$ are the Reynolds number and Péclet number of the flow in micro-capillary of radius $r_i$, respectively. $D_{\mathrm{m}}$ [$\mathrm{m}^2/\mathrm{s}$] is the coefficient of molecular diffusion. We note that Eq. 34, 35, 36, and 37 can be used to estimate upscaled effective Darcy shear stress, effective Darcy shear rate, effective Reynolds number and effective Péclet number of the Newtonian fluid, respectively, by equating $\eta_{\mathrm{eff,i}} = \mu$ and $\beta_{\mathrm{f}} = 1$. We note that effective parameters defined above takes into account the pore-scale variation in these values due to variation in the pore-size in the porous medium, thus, these values could be considered as representative values (*i.e.* upscaled values) for a given set of conditions.

## 4. Numerical approach

We simulated the flow of non-Newtonian fluid modelled using Meter model and viscoelastic linear PTT model through void spaces using finite volume method based OpenFOAM C++ libraries [72] and compared the results with a bundle-of-capillary model (BCM) for non-Newtonian fluids. The volume-averaged values over a porous medium domain obtained after numerical simulation are considered as upscaled value for comparison to the Darcy's scale.

### *4.1. Meter model*

To implement Meter model in OpenFOAM, we convert the Meter model in terms of shear rate by substituting $\tau = \eta_m \dot{\gamma}$ in Eq. 11, where $\eta_m = \dfrac{\eta_0 + \eta_\infty}{2}$ is the viscosity of the fluid at $\tau_m$. This leads to corresponding change in exponent of Meter model to $S^{-1}$. The Meter model will be as in

Eq. 38,

$$\eta = \eta_\infty + \frac{\eta_0 - \eta_\infty}{1 + \left(\frac{\eta_0 + \eta_\infty}{2\,\tau_m}\,\dot{\gamma}\right)^{S^{-1}}} \tag{38}$$

The continuity equation (Eq. 6), momentum equation (Eq. 7) along with Meter model equation (Eq 38) was solved using OpenFOAM 7. We used PIMPLE (i.e. merged PISO-SIMPLE) algorithm of OpenFOAM to solve the pressure-velocity coupling with 8 nOuterCorrectors and increase the accuracy of the results [73]. The Semi-Implicit Method for Pressure-linked equation (SIMPLE) algorithm [74] can calculate only steady-state solutions, on the contrary, Pressure-Implicit Splitting Operator (PISO) algorithm takes into account velocity correction term which was neglected in SIMPLE algorithm [73, 75]. Readers are refers to the [73, 74, 75, 76] for more details on SIMPLE, PISO and PIMPLE algorithm. The second-order implicit backward method was used to discretise the time scheme of the governing equations. The gradient term and divergence term were discretised using Gauss linear scheme of OpenFOAM, which uses standard finite volume Gaussian integration. The Gauss linear uncorrected scheme of OpenFOAM was employed to discretise Laplacian term of governing equations. The system of equations obtained after discretisation was solved using iterative matrix solvers. We computed the pressure field using Generalised Geometric-Algebraic Multi Grid (GAMG) solver with diagonal incomplete-Cholesky (symmetric) smoother. The velocity profile was determined using smoothSolver of OpenFOAM with a Gauss-Seidel smoother. We applied the convergence criteria of $10^{-6}$ for pressure and velocity field. The time-step of $10^{-7}$ s was applied to maintain a Courant number (C) below 0.01 during the simulation. The Courant number is defined as $C = \frac{u\,\Delta t}{\Delta x}$, where, $\Delta t$ is the time step and $\Delta x$ is length interval. The magnitude of shear

rate and shear stress in flow field was determined using Eq. 9 and Eq. 10, respectively.

### *4.2. Linear Phan–Thien—Tanner model*

We used RheoTool [77], which is implemented in the OpenFOAM, to simulate linear PTT fluid flow. RheoTool uses the Semi-Implicit Method for Pressure-linked equation (SIMPLEC) algorithm for pressure-velocity coupling [64]. Pimenta and Alves [64] developed a new method for stress-velocity coupling which is second-order accurate and implemented in RheoTool [77]. We used preconditioned conjugate gradient solver to estimate the pressure and velocity field, whereas, preconditioned (bi-) conjugate gradient (PBiCG) solver was utilised to estimate stress field. The Gauss linear corrected scheme was used to discretise Laplacian term and Gauss linear scheme to discretise gradient and divergence term of governing equations. Convergent and Universally Bounded Interpolation Scheme for the Treatment of Advection (CUBISTA) scheme was used for convective term [78, 77, 64] of the governing equation. Readers are referred to [64, 77] for detailed information on available methods to solve linear PTT model using RheoTool.

### *4.3. Numerical domain and boundary conditions*

We conducted three sets of numerical experiments. In the first set, we used microfluidic experimental data of Galindo-Rosales *et al.* [53] to validate numerical simulation approach adopted in the present work. In the second set, we simulated the Meter model fluid flow through 2D porous medium (Fig 1c) over a pressure gradient range and compared it with a BCM. In the third set, we simulated Newtonian fluid, Meter model fluid, and linear PTT fluid flow through heterogeneous Mt Simon sandstone (Fig

1e) and compared them with BCM. Fig 1 shows the porous medium domain's geometry along with pore-size distribution and boundary conditions. We applied wall boundary condition at the top, bottom, front, back and solid surface of 3D domain with no-slip velocity and zero fixed flux pressure. The right boundary had total pressure and zero flux corrected velocity boundary conditions.

To validate numerical simulation approach adopted in the present work for the flow of Meter model fluid and linear PTT fluid in a porous medium, we used experimental data of Galindo-Rosales *et al.* [53]. Similar to Galindo-Rosales *et al.* experiments, we simulated flow of polyacrylamide (PAA, 50 ppm) fluid through symmetric micro-channel (Fig 1a.) in 3D over a range of Deborah numbers (0.01 - 5). We applied a constant injection rate boundary condition at the inlet (left boundary). Readers are referred to [53] for more details on experiments. Similar to [53], we defined Deborah number as $De = \lambda \frac{U}{l}$, where, $\lambda$ is the longest relaxation time and $l$ is the characteristic length scale.

In the second set of numerical experiment, we simulated flow of the 0.50% PAA fluid of [71] modelled using Meter model through a 2D porous medium ($\phi = 0.38$) over a range of pressure gradient values ($10^2$ - $10^8$ Pa/m). We applied a constant pressure gradient at the left boundary (inlet) of the 2D porous medium (Fig. 1c).

In the third set, we simulated the flow of Newtonian fluid (water, $\mu =$ 0.001 Pa·s) and 50 ppm PAA fluid of [53] modelled using Meter model and linear PTT model through heterogeneous Mt. Simon sandstone ($\phi = 0.24$) of [79] in 3D. We applied constant injection velocity at the left boundary of Mt Simon sandstone.

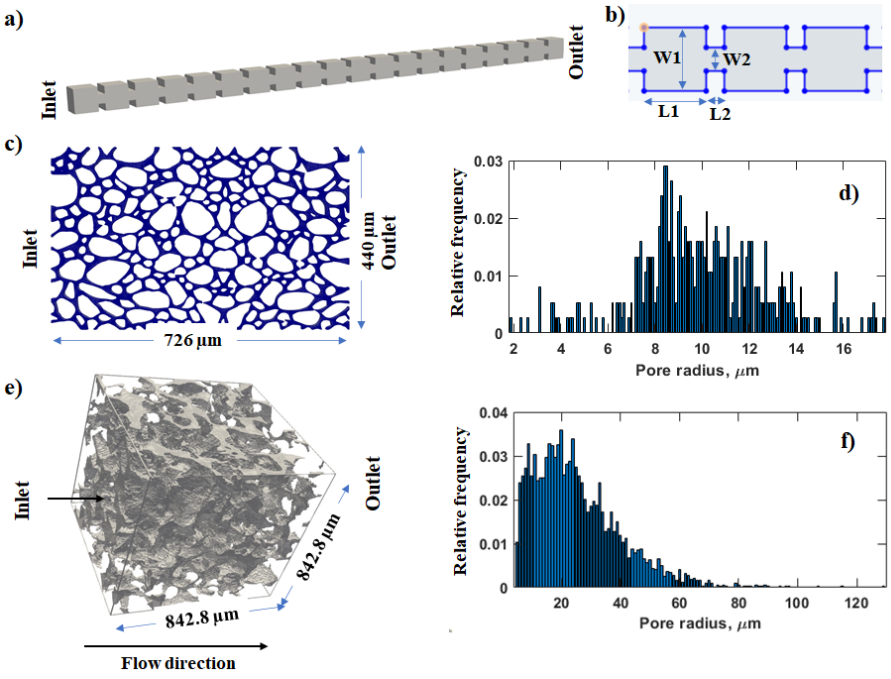


Figure 1: (a) Symmetric micro-channel with 20 repetitive elements of (b) with size : L1 = 106 $\mu$m, L2 = 32 $\mu$m, W1 = 108 $\mu$m, W2 = 40 $\mu$m, H = 103 $\mu$m, (c) 2D porous medium of size 726 $\mu$m $\times$ 440 $\mu$m, (d) pore-size distribution of 2D porous medium, (e) segmented Mt Simon sandstone of size 842.8 $\mu$m $\times$ 842.8 $\mu$m $\times$ 842.8 $\mu$m, and (f) pore-size distribution of Mt Simon sandstone. Fluid flows from left to right. No-slip condition at solid surfaces and boundaries (except at inlet and outlet).

### *4.4. Image processing and visualisation*

We used Fiji ImageJ software [80] to process images and Paraview 5.7.0 software to visualise and post-process the fluid flow profile data. We used micro-CT scan data of Mt Simon sandstone of Kohanpur *et al.* [79] which is available at Digital Rock portal [81]. The details of the micro-CT scan of Mt. Simon sandstone (original size 3.363 $mm^3$) is given in Kohanpur *et al.* [79]. Voxel size of the segmented micro-CT sample is 2.8 $\mu$m. We took sub-sample of size 301×301×301 voxel (*i.e.* 842.8 $\mu$m × 842.8 $\mu$m × 842.8 $\mu$m) from original Mt. Simson sandstone for present work to minimise computational expenses. The pore-spaces from images were extracted and saved in the required stereolithography (STL) format using '3D Viewer' plugin [80] of imageJ. The mesh in the pore-space of the extracted STL file was generated using snappyHexMesh module of OpenFOAM. We determined pore-size distribution and porosity of the porous medium using the method proposed by Rabbani and Salehi [82].

We computed the fluid flow rate at the right boundary of the porous medium using SurfaceFlow filter of the Paraview, which integrates the fluid's velocity over the surface at the outlet. We computed average velocity through the porous medium by dividing the estimated flow rate by total cross-section area of the porous medium at the outlet boundary. We used the "Integrate variable" filter of Paraview to estimate pore-scale volume-averaged velocity, shear rate, shear stress, and viscosity over the porous medium domain. These volume-averaged values can be considered as up-scaled values. We simulated flow of water through porous medium using OpenFOAM to determine the intrinsic permeability of the porous medium (using Eq. $k = \frac{U_N \mu}{\frac{dP}{dx}}$).

### *4.5. Assumptions and Limitations*

Meter model is an empirical equation that gives the best fit of shear

viscosity – shear stress data. These data are measured using a rheometer and are susceptible to measurement errors. Meter model equation does not consider viscoelasticity (*e.g.*, relaxation time, normal stress, and shear modulus) of the fluids. The linear PTT model defines the extra stress tensor of the fluid flow theoretically. For instance, the relaxation time of non-Newtonian fluid varies with the applied stress; however, linear PTT model considers the longest relaxation time in its formulations. The viscoelastic fluid flow simulation modelled using PTT has numerical stability issues. We have used both-side-diffusion technique implemented in rheotool to address the stability issue in PTT fluid flow simulations. The readers are referred to [83] which compares different approaches available in the literature to stabilize viscoelastic fluid flow simulation. Readers are also referred to [1, 9, 64, 77] for detailed information on the assumption and limitation of GNF and viscoelastic fluid flow simulations. Although these models are developed based on certain assumptions and have limitations, they provide certain understandings about the fluid dynamics of non-Newtonian fluids.

## 5. Results and discussion

### *5.1. Analytical solutions*

Fig. 2 shows that an experimental velocity profile of Escudier et al. (2005) [84] gave a good fit with the analytical solution of MM (Eq. 12) and linear PTT (Eq. 18) models for radial velocity profile at the pressure gradients of 37.5 Pa/m during the flow of 0.125% polyacrylamide through the pipe of radius 5 cm. We note that the rheological parameters of Phan–Thien—Tanner model were absent in the [84] work; thus, we considered zero-shear viscosity ($\eta_0$) of PAA as polymer viscosity of the linear PTT $\eta_\mathrm{p} = 0.2257$. The characteristic time of Meter model [63] (i.e $\lambda = \frac{\eta_0+\eta_\infty}{2\,\tau_\mathrm{m}} = 0.47$ s) was considered as the longest relaxation time of PAA

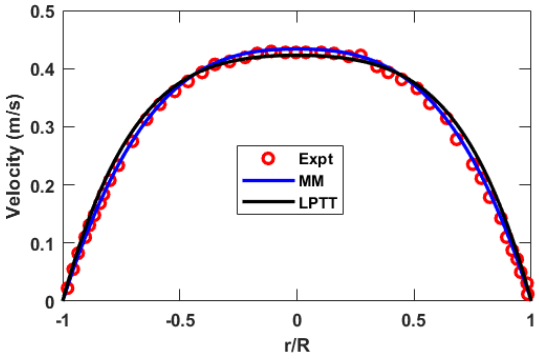


Figure 2: Comparison of experimental radial velocity profile of [84] with analytical solution of Meter model (Eq. 12) and linear Phan–Thien—Tanner (Eq. 18) during flow of a 0.125% polyacrylamide (PAA) fluid through a circular tube (radius 0.05 m) [Meter model parameters: $\eta_0 = 0.2257$ Pa·s, $\eta_\infty = 0.000896$ Pa·s, $\tau_{\mathrm{m}} = 0.2381$ Pa, $S = 1.2$ [63]; linear PTT model parameters: $\eta_{\mathrm{p}} = 0.2257$ Pa·s, $\lambda = 0.47$ s, $\varepsilon = 0.65$]

fluid. The $\varepsilon$ parameter of linear PTT model was considered as the fitting parameter for velocity profile. $\varepsilon$ value of 0.65 gave a good fit with an experimentally observed velocity profile of [84] as shown in Fig 2.

These results imply that the Meter model parameters and the Meter model's analytical solution for velocity profile can be utilised to determine the unknown parameters of the linear PTT model. Thus, we have adopted the same approach to determine linear PTT model parameters from Meter model parameters of PAA fluid in the subsequent work.

### *5.2. Validation of BCM using experimental observation*

We utilised experimental data of 0.5% Separan AP30 (polyacrylamide, PAA) fluid flow in a packed bed of glass beads [71] to validate the Bundle-of-Capillaries model (BCM) for non-Newtonian fluids approach proposed in the present work. Fig. 3a shows a perfect fit of shear viscosity data of [71] with the Meter model (Eq. 11). The Meter model parameters and linear

PTT model parameters are given in the description of the Fig. 3. Linear PTT parameters were determined using Meter model parameters and comparing the MM and linear PTT model's analytical solution described in Section 5.1. Due to absence of the packed beds pore-size distribution and tortuosity data in [71], we utilised the sand-pack pore-size distribution of [24] as shown in Fig 3b and sand-pack tortuosity value of 1.4 [85] in the present work. We computed $\beta_{\mathrm{p}} = 11.56$ of the sand-pack using Eq. 24 and adopting permeability value ($k = 3.57 \times 10^{-9}$ m$^2$) of [71] packed bed. The estimated $\beta_{\mathrm{f}} = 0.79$ for Meter model fluid and $\beta_{\mathrm{f}} = 0.75$ for linear PTT model implies that the non-Newtonian fluid alters geometry of the pore-structure due to either adsorption, deposition of polymers/colloidal suspension, pore blockage or viscoelastic instability. We note that the $\beta_{\mathrm{p}}$ and $\beta_{\mathrm{f}}$ are pore-scale parameters which take into account the pore-scale variability due to geometry of the pore space and fluid rheology, thus, different porous medium and fluids will have different $\beta$ values.

Fig. 3c and Fig. 3d depict that the Darcy velocity estimated using Eq. 28 and Darcy viscosity estimated using Eq. 31 in the packed bed match closely with the experimentally measured data of Park *et al.* [71]. Furthermore, Fig. 3e depicts a good fit of the experimentally measured shear viscosity - shear stress data (measured using rheometer) [71] with the Darcy viscosity-effective shear stress estimated using BCM (Eq. 31 and Eq. 34). Likewise, Fig. 3f shows a good match of the experimental shear rate-shear stress with an effective Darcy shear rate-effective Darcy shear stress estimated using Eq 34 and Eq 35 of BCM respectively. These results are an improvement to the reported methods in literature (*e.g.*. [71, 24, 86, 15, 16]) wherein the shift factor $\alpha$ was applied to match the shear rate-dependent viscosity measured using rheometer with the Darcy viscosity in porous medium. The mismatch observed in the previous works

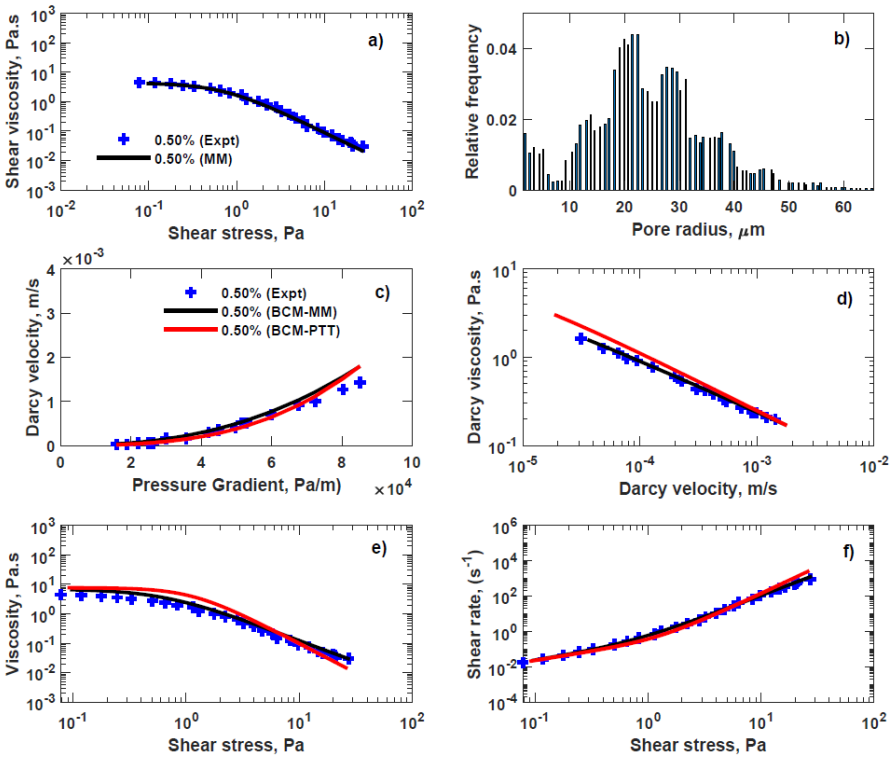


Figure 3: (a) Experimental shear viscosity-shear stress of 0.5% Separan AP30 fluid of [71] modelled using Meter model (MM, Eq. 11), (b) sandpack network pore size distribution of [24], (c) experimentally measured Darcy velocity as a function of pressure gradient [71] compared with velocity estimated using Eq. 29, (d) experimental Darcy viscosity compared with Darcy viscosity estimated using Eq. 31, (e) experimental shear viscosity as a function of shear stress (measured using rheometer) compared with Darcy viscosity and effective shear rate estimated using Eq. 31 and Eq. 35, and (f) experimental shear rate as a function of shear stress (measured using rheometer) compared with the effective shear rate and effective shear stress estimated using Eq. 34 and Eq. 35. BCM-MM: Bundle-of-capillary model for Meter model fluid; BCM-PTT: Bundle-of-capillary model for linear Phan–Thien—Tanner model fluid. Meter model parameters: $\eta_0 = 4.35$ Pa·s, $\eta_\infty = 0.001$ Pa·s, $\tau_{\rm m}= 0.718$ Pa, $S = 1.471$; linear PTT model parameters: $\eta_{\rm p} = 4.35$ Pa·s, $\lambda = 3$ s, $\varepsilon = 0.6$.

was due to the simplified assumption of a Bundle-of-Capillaries model based Carman–Kozeny equation that does not consider the pore-size distribution and alteration in the effective pore radius due to polymeric adsorption, desorption and viscoelasticity.

The analytical solution of linear PTT model derived by [62] does not consider the contribution of solvent viscosity. This could be the reason for the slight deviation of linear PTT based BCM estimate from the experimental observations, as shown in Fig. 3. However, Meter model based BCM estimate closely matches with experimental observations.

Fig. 4 compares effective Reynolds number estimated using Eq. 36 with the volumetric flow rate of MM fluid and linear PTT fluid in porous medium estimated using Eq. 33. Fig. 4 implies that even though effective Reynolds number of the non-Newtonian fluid is lower than 1.67, the volumetric flow rate is non-linearly dependent on the effective Reynolds number. This non-linearity is due to the elasticity of non-Newtonian fluids [16, 7, 70]. The proposed BCM correctly captures changes observed during non-Newtonian fluids' flow due to elasticity through $\beta_{\mathrm{f}}$.

Park *et al.* [71] estimated Reynolds number based on particle diameter ranged from $6 \times 10^{-5}$ to 0.93 for packed bed, on the contrary effective Reynolds number estimated using Eq 36 of BCM for the same experimental data ranged from $7.2 \times 10^{-5}$ to 1.67 (Fig. 4). Park *et al.*'s Reynolds number is based on representative particle diameter; on the contrary, BCM based Reynolds number is an average Reynolds number of the fluid in capillaries. This suggests that $Re_{\mathrm{eff}}$ estimated using BCM is representative $Re_{\mathrm{eff}}$ for non-Newtonian fluids in the porous media compared to the $Re$ formulation developed based on the particle diameter. Rodríguez de Castro and Radilla [86] experimentally observed similar non-linear relationship between $Re_{\mathrm{eff}}$ and volumetric flow rate for non-Darcy flow of xanthan gum fluids in the

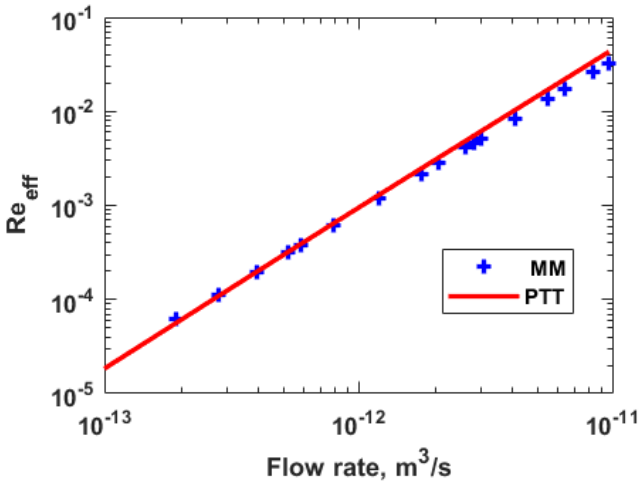


Figure 4: Effective Reynolds number ($Re_{\text{eff}}$) estimated using BCM (Eq. 36) over a range of experimentally observed flow-rate values of [71] during flow of 0.5% PAA fluid through a packed bed.

fractured granite and the Vosges sandstone.

### *5.3. Direct numerical simulation (DNS)*

#### *5.3.1. Validation of numerical simulations*

Galindo-Rosales *et al.* experimental measurements [53] during the flow of shear-thinning 50 ppm polyacrylamide (PAA) fluid in symmetric micro-channel were used to validate numerical simulation approach adopted in the present work for the flow of Meter model fluids and linear PTT model fluid in the porous medium. Fig. 5a shows a statistically good fit of experimental shear viscosity data of [53] with the Meter model (Eq. 11). The Meter model parameters and linear PTT parameters are given in the description of Fig. 5. The characteristic time of Meter model (0.054 s) was similar to the relaxation time measured by Galindo-Rasales *et al.* using capillary break-up extensional rheometer (CaBER). The parameter $\varepsilon$ was determined

using an analytical solution of linear PTT and Meter model.

We adopted 3D simulation domain similar to Galindo-Rosales *et al.* [53] (see Fig. 1a,b). The fine mesh with over 10 million mesh points was generated using snappyHexMesh in the microchannel domain. We applied a constant injection rate at the inlet and allowed the flow to reach statistically steady-state. Fig. 5b shows that experimentally observed pressure gradient-Deborah number closely matches the numerical simulations of the Meter model and linear PTT model. However, the Meter model's streamline could not match the experimental observation of Galindo-Rosales *et al.* (see Fig. 5). Linear PTT model takes into account the elasticity of the fluid; thus, Fig. 5 depicts that streamlines reported by Galindo-Rosales closely match with streamlines of linear PTT model simulations for similar fluid flow conditions. Similar to experimental observation, simulation using linear PTT model shows vortex formation even at lower Deborah numbers. The vortex size increased at the corner with an increase in Deborah number (see Fig 5f,g,h).

The linear PTT fluid simulation showed chaotic unsteady flow during the initial few seconds with drastic variations in the shape and size of the vortex. However, after a critical time linear PTT fluid reached a statistically-steady state with a relatively same vortex pattern (*i.e.* viscoelastic instability) at the corner. Movie clip 1 of the supporting information (SI) shows this transition of chaotic viscoelastic instability from unsteady state to statistically-steady state instability using velocity vector glyphs for linear PTT fluid flow at De of 0.25. Fig. 5l,m show the profile of velocity and magnitude of stress at the micro-channel centre over a simulation domain. Fig. 5l,m depict that velocity and magnitude of stress at the throat are much larger than the other regions of the micro-channel domain.

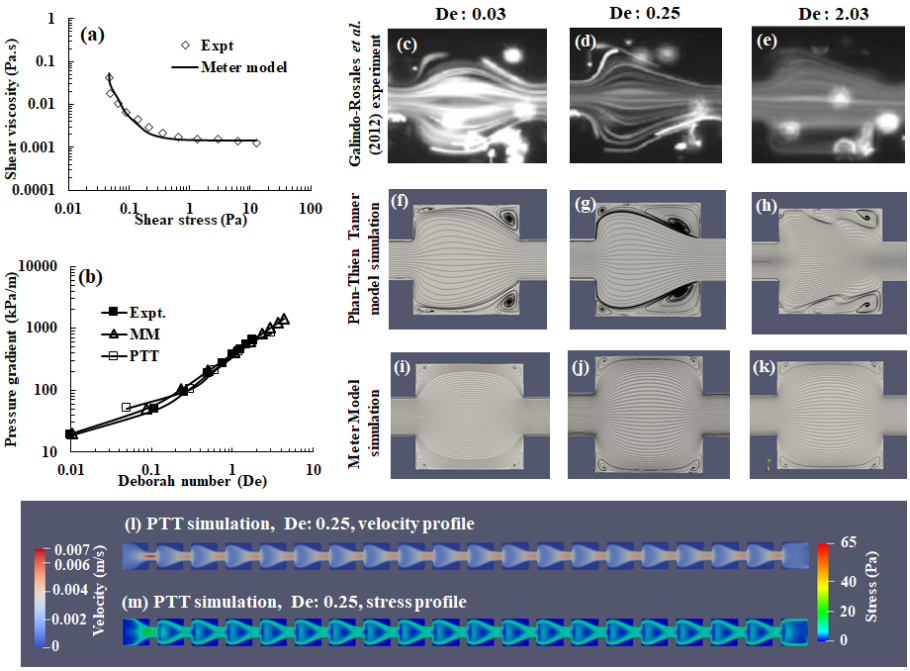


Figure 5: Comparison of the streamline data obtained after numerical simulation of the flow of 50 ppm PAA fluid (modelled using Meter model and linear PTT model) in symmetric microchannel geometry with the experimental streamline data reported by Galindo-Rasales *et al.* [53] over a range of Deborah numbers. (a) Shear viscosity - shear stress (50 ppm PAA solution, Meter model parameter: $\eta_0 = 0.11$ Pa·s, $\eta_\infty = 0.0014$ Pa·s, $\tau_m = 1.07$ Pa, $S = 1.2$); linear PTT model parameters: $\eta_\mathrm{p} = 0.11$ Pa·s, $\eta_\mathrm{s} = 0.001$ Pa·s, $\lambda = 0.054$ s, $\varepsilon = 0.3$, $\zeta = 0.02$. (b) Comparison of experimentally observed pressure gradient as a function of Deborah numbers with numerical simulation of PAA fluid modelled using Meter model and linear PTT model. (c,d,e) Experimentally observed streamline snapshot of Galindo-Rosales *et al* [53]. (f,g,h) Streamlines of the flow obtained after linear PTT model numerical simulations. (i,j,k) Streamline of the flow obtained after MM model numerical simulations. (l,m) Velocity profile and magnitude of stress profile at De = 0.25 during linear PTT model fluid.

These results imply that the linear PTT model gives a more accurate description of pore-scale fluid flow behaviour than the Meter model. However, the average values of the stress, shear rate, velocity, and pressure gradient in the linear PTT model and Meter model's simulation domain are comparable, with slight variation.

*5.3.2. Polymeric fluid flow in a 2D porous medium*

Fig 1c shows pore structure of the 2D micro-porous medium of size 726 $\mu$m $\times$ 440 $\mu$m [87]. The pore size distribution (Fig 1d) and the porosity of 38% are as shown in Fig 1d. We simulated flow of 0.5% PAA fluid of [71] modelled using Meter model over a range of pressure gradient values ($1.38\times10^{2}$ - $1.38\times10^{8}$ Pa/m). The intrinsic permeability of the 2D porous medium estimated using simulation was 1.32 $\times10^{-12}$ m$^2$. We estimated tortuosity of 1.04 for 2D porous medium by measuring length of streamlines. We obtained $\beta_{\mathrm{p}}$ of 0.5215 for the 2D porous medium using pore-size distribution values as given in Fig 1d. The BCM-MM approach gave same volumetric flow rate as obtained using direct numerical simulations over a range of pressure gradient values at the $\beta_{\mathrm{f}} = 1$.

Fig. 6 depicts the boxplot statistics observed for the distribution of viscosity values in the 2D porous medium over a range of shear stress values. It also compares the mean viscosity obtained using simulations with a viscosity estimated using BCM approach (Eq. 31) and the experimental shear viscosity (measured using rheometer). The experimental shear viscosity of PAA of [71] for a given shear value was estimated using the Meter model. The figure shows many outlier viscosity values (marked in red plus sign) at higher shear values. These values represent the fluid's viscosity in the immobile (stagnant) zones, which do not contribute to the fluid's active flow in the porous medium. It also shows that average viscosity values lie

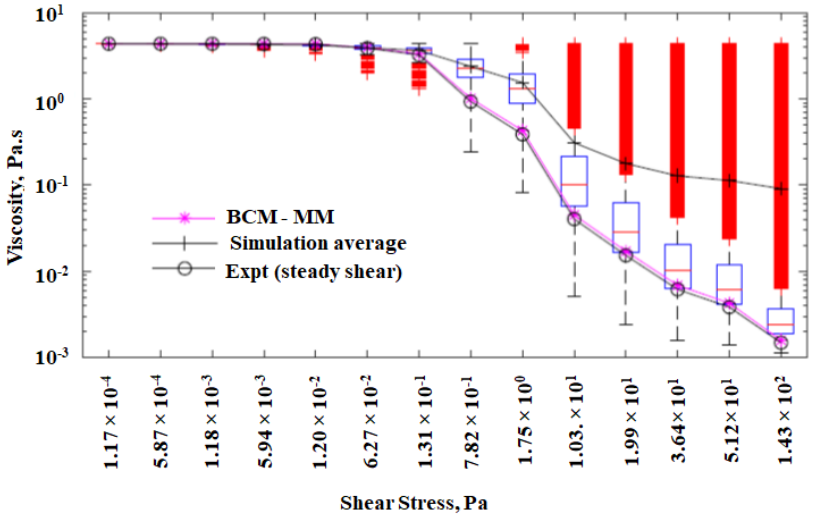


Figure 6: The boxplot of the viscosity as a function of shear stress during flow of Meter model fluid through 2D porous medium. The boxplot statistics is compared with the values obtained using BCM approach (Eq. 31) and experimental shear viscosity values (measured using rheometer). red plus signs indicate outlier values.

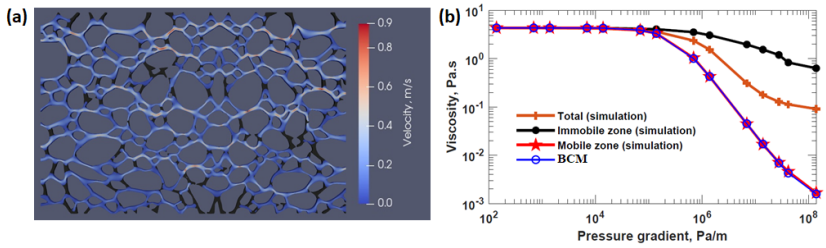


Figure 7: (a) Immobile zone (marked in a black colour) and velocity profile in a mobile zone (marked in red - white - blue colour) at a pressure gradient of 138 MPa/m, and (b) average viscosity in the total porous medium domain, immobile (stagnant) zone, and mobile zone obtained using BCM and DNS.

in the upper outlier region of the boxplot.

To explore further, similar to the approach adopted by de Anna *et al.* [52], we define the immobile zone (or stagnant zone) as the pore space region which has pore-velocity two orders of magnitude lower compared to the average pore-velocity in the porous medium domain and rest of the pore-space region as the mobile zone. We segmented the porous medium domain in the high pore-velocity mobile zone and low pore-velocity immobile (stagnant) zone, as shown in Fig 7a. We observed that the immobile zone was 14% of the porous medium domain over a range of pressure gradients ($1.38 \times 10^2$ Pa/m, $1.38 \times 10^4$ Pa/m, $1.38 \times 10^6$ Pa/m, and $1.38 \times 10^8$ Pa/m). Fig 7 depicts that most immobile zones are either dead-end of the pore-spaces or perpendicular to the applied pressure gradient and active fluid flow direction. Fig 7b shows a comparison of the average viscosity of the fluid in the porous medium domain, its mobile zone, its immobile stagnant zone (obtained after numerical simulation) and the Darcy viscosity (estimated using BCM approach) over a range of pressure gradients. These results show that the average viscosity of the fluid in the immobile zone is very high compared to the mobile zone. Moreover, viscosity of the fluid in

the mobile zones closely matches with the Darcy viscosity of the fluid in the porous medium estimated using BCM approach. These results imply that the Darcy viscosity of the fluid represents the viscosity of fluid in the mobile zone of porous medium only.

*5.3.3. Flow in Mt. Simon sandstone*

To explore the effectiveness of the Bundle-of-Capillaries model for non-Newtonian fluids, we simulated the flow of water, and 50 ppm PAA fluid of [53], modelled using Meter model and linear PTT model, through Mt. Simon sandstone at a constant injection rate of $10^{-4}$ m/s. Fig. 1e shows a segmented 3D subsample of Mt. Simon sandstone utilised in the present work. In total 12,112,242 mesh point was generated in the pore-space of Mt. Simon sandstone's subsample using snappyHexMesh module of OpenFOAM. We determined pore-size distribution (Fig. 1f) and porosity of (24 $\pm$ 4 %) of the Mt. Simon sandstone. The porosity of 24% and the degree of anisotropy of 0.255 determined using 'BoneJ' plugin of ImageJ suggests that sandstone subsample is heterogeneous. The average length of streamlines of fluid flow in the Mt. Simon sandstone was 0.001089 m, which gave tortuosity of 1.29.

Table 1 shows estimated average velocity, pressure gradient, and permeability during the flow of water, MM fluid, and linear PTT fluid through Mt. Simon sandstone. The intrinsic permeability of $4.2\times10^{-12}$ m$^2$ estimated in present work using OpenFOAM simulation is close to the permeability of $3.8\times10^{-12}$ to $4.15\times10^{-12}$ m$^2$ estimated by Kohanpur *et al.* [79] using the lattice-Boltzmann method, pore-network method and direct numerical simulations for the subsample of Mt. Simon sandstone. The computed parameters given in the Table 1 are close to the field scale values [12].

Fig 8 shows the comparison of velocity fields and streamlines in 3D

Table 1: OpenFOAM simulation based estimated parameters during flow of Newtonian (water) and 50 ppm PAA fluid through Mt. Simon sandstone.

| Parameter | Water | 50 ppm PAA | |
|---|---|---|---|
| | | MM | PTT |
| Average velocity (m/s) | $1.47\times10^{-4}$ | $1.47\times10^{-4}$ | $1.47\times10^{-4}$ |
| Pressure gradient (MPa/m) | 0.035 | 0.52 | 0.5 |
| Intrinsic permeability ($m^2$) | $4.2\times10^{-12}$ | - | - |

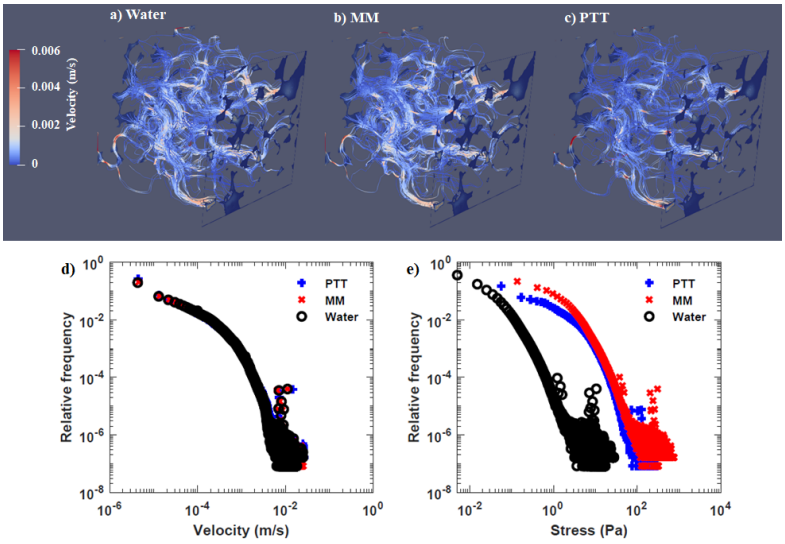


Figure 8: Comparison of the streamline and velocity fields in the Mt Simon sandstone during the flow of (a) water, and 50 ppm PAA fluid of [53] model using (b) Meter model (MM), and (c) linear PTT model. (d) Relative frequency of velocity, and (e) relative frequency of shear stress over 12 million mesh points of Mt Simon sandstone.

during the fully developed steady-state flow of water, PAA fluid modelled using Meter model and linear PTT model in Mt. Simon sandstone at a constant injection rate of $10^{-4}$ m/s. Fig 8 depicts that the flow paths adopted by Water and PAA fluid modelled using Meter model are similar, on the contrary, the flow path adopted by PAA fluid modelled using linear PTT model shows slight deviation compared to Meter model at same injection rate. This slight deviation in the flow path is due to visco-elasticity of the PAA fluid, which linear PTT could capture. Formation of the vortex in the pore-spaces was observed during the PAA fluid flow modelled using linear PTT model at an applied injection rate of $10^{-4}$ m/s. However, we did not observe vortex formation during the flow of water and PAA fluid modelled using Meter model. This implies that the variation of pore-space geometry (*i.e.* converging or diverging) in the heterogeneous Mt. Simon sandstone influences the flow path of a single-phase flow of PAA fluid even if the flow is predominantly laminar. Note that distribution of velocity values over 12 million points in the Mt simon sandstone's pore-space are similar for Water, MM fluid and linear PTT fluid, due to the same injection rate (see Fig 8d).

The relative frequency distribution of velocity profile (Fig 8d) of the PAA fluid in the porous medium follows a similar trend as observed by de Anna *et al.* [8] during the flow of viscoelastic fluid through random porous medium. Although a same injection flow rate was applied at inlet during the flow of water and the PAA fluid, the distinct variations in the stress field exist in an Mt. Simon sandstone for water and PAA fluid (Fig 8e) flow. Berg and Wunnik [12] observed a similar trend for the shear rate field during Newtonian fluid (water) flow through Berea sandstone.

Table 2: Comparison of DNS and BCM estimated parameters during flow of a PAA fluid, modelled using Meter model and linear PTT model, through Mt. Simon sandstone.

| Parameter | BCM | | DNS | |
|---|---|---|---|---|
| | MM | PTT | MM | PTT |
| $\beta_{\mathbf{f}}$ | 1.17 | 1.286 | - | - |
| Average velocity (m/s) | $1.47\times10^{-4}$ | $1.47\times10^{-4}$ | $1.47\times10^{-4}$ | $1.47\times10^{-4}$ |
| Average viscosity (Pa·s) | 0.0143 | 0.0143 | 0.058 | 0.0361 |
| Average stress (Pa) | 2.98 | 3.28 | 2.01 | 1.44 |

*5.3.4. Comparison of BCM approach with DNS*

Table 2 compares the estimated values using direct numerical simulation and BCM approach during the flow of PAA fluid through Mt. Simon sandstone. We obtained $\beta_{\mathrm{p}}$ of 0.4018 for Mt. Simon sandstone using pore-size distribution values as given in Fig 1f, porosity of 24%, tortuosity of 1.3 and intrinsic permeability of $4.2\times10^{-12}$ $\mathrm{m}^2$. The $\beta_{\mathrm{f}}$ parameters as given in the Table 2 gave volumetric flow rate of $1.6648\times10^{-12}$ $\mathrm{m}^3/\mathrm{s}$ at the outlet similar to the volumetric flow rate obtained using direct numerical simulations of PAA fluid modelled using Meter model and linear PTT model.

Table 2 shows that the estimated values for average viscosity, average shear rate and average stress using BCM are different from those obtained using direct numerical simulations. Since viscosity, shear rate and stress values are distributed in the Mt. Simon sandstone; the average values estimated using DNS may not be representative values for Darcy scale flow as described in Section 5.3.2. Thus, effective shear rate, effective shear stress and Darcy viscosity estimated using BCM could be considered the representative values for Mt. Simon sandstone. We note that the average shear stress values of BCM are relatively close to the values estimated using DNS.

The Mt. Simon sandstone's viscosity values vary from 0.009 to 0.11

Pa·s with an average value of 0.058 Pa·s during Meter model fluid flow. On the contrary, Darcy viscosity estimated using BCM is 0.0143 Pa·s. To examine the reason for this drastic variation, we segmented flow zone into the mobile and immobile zone as described in section 5.3.2. We obtained mean viscosity of 0.014 Pa·s and 0.09 Pa·s in the mobile zone and immobile (stagnant) zone in the Mt. Simon sandstone. 25% of the volume was an immobile zone in the Mt. Simon sandstone. The average viscosity in the mobile zone closely matches with the Darcy viscosity estimated using BCM. These results further strengthen that the Darcy viscosity is the non-Newtonian fluid's viscosity in the active mobile zone of the porous medium.

## 6. Conclusions

We defined the pore-correction coefficient $\beta_{\mathrm{p}}$ of a micro-capillary during Newtonian fluid flow and the fluid-correction coefficient $\beta_{\mathrm{f}}$ for correcting the pore geometry of micro-capillary due to fluid rheology during non-Newtonian fluid flow. The proposed model takes into account the effect of variation of geometric properties of porous medium and the effects of non-Newtonian fluids on the hydraulic conductivity of the fluid in the porous media. The proposed BCM formulations for upscaled Darcy viscosity, effective Darcy shear rate, and effective Darcy shear stress do not depend on the empirical shift factor ($\alpha$). Most of the recent works (*e.g.*, [12, 23, 25]) were focused on identifying relationship between $\alpha$ with pore-morphology and fluid rheology. The BCM model approach differentiates the effect of pore structure (using $\beta_{\mathrm{p}}$) and the effect of fluid rheology (using $\beta_{\mathrm{f}}$) on the behaviour of the fluid flow in porous medium. While $\alpha$ is an empirical fitting parameter that is being used to correct the Darcy shear rate value of the porous medium, $\beta_{\mathrm{p}}$ and $\beta_{\mathrm{f}}$ are directly related to the physical parameters, *i.e.* pore morphology, of a porous medium, respectively.

We have also shown that the shear viscosity in rheometer and Darcy viscosity in porous media under given shear values are similar. The effective Reynolds number formulation proposed in the present work represents Reynolds number of non-Newtonian fluids flow in the porous medium compared to the Reynolds number proposed based on particle diameters and Blake-Kozeny equations.

Moreover, we simulated non-Newtonian fluid flow (modelled using shear stress-dependent Meter model and linear Phan-Thien Tanner model) through porous medium using the finite volume method based on OpenFOAM C++ libraries. We have shown that the Phan-Thien Tanner model gives a more accurate pore-scale description of the fluid flow than the Meter model. However, the upscaled values of both Meter model and linear PTT model are comparable.

The flow fields of viscosity and shear stress obtained after direct numerical simulation of the flow of polymeric PAA fluid and Newtonian fluid show that the pore space geometry of porous medium affects the fluid flow behaviour. The volume-averaged shear rate, average shear stress and average velocity obtained after direct numerical simulation closely match the proposed Bundle-of-Capillaries for the non-Newtonian fluids approach developed for the Meter model and linear PTT viscoelastic model. However, the porous medium's immobile and mobile zones affect rheology, so that the Darcy viscosity of the fluid associates with the viscosity of the fluid in the active mobile zone of porous medium only.

Direct numerical simulation is computationally expensive and, consequently, cannot be directly applied to the field scale applications, *e.g.* enhanced oil recovery. The upscaled macroscopic parameters using BCM approach could be utilised for Darcy scale simulation. This will be our future interest. Another line of research is two-phase flow modelling at pore

scale using the Meter model and experimental microfluidic data [88], and differentiate the impact of different flow zones on upscaled viscosity from pore scale.

## Supporting Information (SI)

The SI includes: Movie clip of linear LPTT fluid flow at Deborah number 0.25.

## Acknowledgement

T.S. gratefully appreciates Rajashri Shahu Maharaj Foreign Scholarship, Government of Maharashtra, India that has enabled him to undertake PhD research at the University of Manchester. The authors would like to acknowledge the assistance given by Research IT and the use of the Computational Shared Facility at the University of Manchester.

## Conflict of interests

The authors declare that they have no conflict of interest.

## References

[1] R. B. Bird, R. Armstrong, O. Hassager, Fluid mechanics, dynamics of polymeric liquids, Vol. 1 (1987).

[2] J. Savins, Non-newtonian flow through porous media, Industrial & Engineering Chemistry 61 (10) (1969) 18–47.

[3] K. S. Sorbie, Polymer-improved oil recovery, Springer Science & Business Media, 2013.

[4] C. Xie, W. Lv, M. Wang, Shear-thinning or shear-thickening fluid for better EOR?—a direct pore-scale study, Journal of Petroleum Science and Engineering 161 (2018) 683–691.

[5] J. Patel, B. Maji, N. H. N. Moorthy, S. Maiti, Xanthan gum derivatives: review of synthesis, properties and diverse applications, RSC Advances 10 (45) (2020) 27103–27136.

[6] K.-W. Song, Y.-S. Kim, G.-S. Chang, Rheology of concentrated xanthan gum solutions: Steady shear flow behavior, Fibers and Polymers 7 (2) (2006) 129–138.

[7] D. Kawale, E. Marques, P. L. Zitha, M. T. Kreutzer, W. R. Rossen, P. E. Boukany, Elastic instabilities during the flow of hydrolyzed polyacrylamide solution in porous media: effect of pore-shape and salt, Soft Matter 13 (4) (2017) 765–775.

[8] S. De, J. Kuipers, E. Peters, J. Padding, Viscoelastic flow simulations in random porous media, Journal of Non-Newtonian Fluid Mechanics 248 (2017) 50–61.

[9] M. Alves, P. Oliveira, F. Pinho, Numerical methods for viscoelastic fluid flows, Annual Review of Fluid Mechanics 53 (2021) 509–541.

[10] R. B. Bird, P. J. Carreau, A nonlinear viscoelastic model for polymer solutions and melts—I, Chemical Engineering Science 23 (5) (1968) 427–434.

[11] R. O. Afolabi, G. F. Oluyemi, S. Officer, J. O. Ugwu, Hydrophobically associating polymers for enhanced oil recovery–part B: A review of modelling approach to flow in porous media, Journal of Molecular Liquids (2019) 111495.

[12] S. Berg, J. van Wunnik, Shear rate determination from pore-scale flow fields, Transport in Porous Media 117 (2) (2017) 229–246.

[13] A. Rodríguez de Castro, M. Agnaou, Numerical investigation of the apparent viscosity dependence on darcy velocity during the flow of shear-thinning fluids in porous media, Transport in Porous Media (2019) 1–28.

[14] A. Rodríguez de Castro, M. Agnaou, A. Ahmadi-Sénichault, A. Omari, Numerical investigation of Herschel-Bulkley fluid flows in 2D porous media: yielding behaviour and tortuosity, Computers & Chemical Engineering (2020) 106922.

[15] A. Rodríguez de Castro, G. Radilla, Flow of yield stress and Carreau fluids through rough-walled rock fractures: Prediction and experiments, Water Resources Research 53 (7) (2017) 6197–6217.

[16] A. Rodríguez de Castro, M. Oostrom, N. Shokri, Effects of shear-thinning fluids on residual oil formation in microfluidic pore networks, Journal of Colloid and Interface science 472 (2016) 34–43.

[17] T. Sochi, Flow of non-newtonian fluids in porous media, Journal of Polymer Science Part B: Polymer Physics 48 (23) (2010) 2437–2767.

[18] C. L. Perrin, P. M. Tardy, K. S. Sorbie, J. C. Crawshaw, Experimental and modeling study of newtonian and non-newtonian fluid flow in pore network micromodels, Journal of Colloid and Interface Science 295 (2) (2006) 542–550.

[19] A. Skauge, N. Zamani, J. Gausdal Jacobsen, B. Shaker Shiran, B. Al-Shakry, T. Skauge, Polymer flow in porous media: Relevance to enhanced oil recovery, Colloids and Interfaces 2 (3) (2018) 27.

[20] T. Tosco, D. L. Marchisio, F. Lince, R. Sethi, Extension of the Darcy–Forchheimer law for shear-thinning fluids and validation via pore-scale flow simulations, Transport in Porous Media 96 (1) (2013) 1–20.

[21] M. Zhang, M. Prodanović, M. Mirabolghasemi, J. Zhao, 3d microscale flow simulation of shear-thinning fluids in a rough fracture, Transport in Porous Media 128 (1) (2019) 243–269.

[22] M. T. Balhoff, K. E. Thompson, A macroscopic model for shear-thinning flow in packed beds based on network modeling, Chemical Engineering Science 61 (2) (2006) 698–719.

[23] F. Zami-Pierre, R. de Loubens, M. Quintard, Y. Davit, Polymer flow through porous media: numerical prediction of the contribution of slip to the apparent viscosity, Transport in Porous Media 119 (3) (2017) 521–538.

[24] X. Lopez, Pore-scale modelling of non-newtonian flow, Ph.D. thesis, University of London (2004).

[25] N. Zamani, I. Bondino, R. Kaufmann, A. Skauge, Computation of polymer in-situ rheology using direct numerical simulation, Journal of Petroleum Science and Engineering 159 (2017) 92–102.

[26] F. Zami-Pierre, R. De Loubens, M. Quintard, Y. Davit, Transition in the flow of power-law fluids through isotropic porous media, Physical Review Letters 117 (7) (2016) 074502.

[27] U. Eberhard, H. J. Seybold, M. Floriancic, P. Bertsch, J. Jiménez-Martínez, J. S. Andrade Jr, M. Holzner, Determination of the effective viscosity of non-newtonian fluids flowing through porous media, Frontiers in Physics 7 (2019) 71.

[28] S. Matsuhisa, R. B. Bird, Analytical and numerical solutions for laminar flow of the non-Newtonian Ellis fluid, AIChE Journal 11 (4) (1965) 588–595.

[29] T. Sochi, M. J. Blunt, Pore-scale network modeling of ellis and Herschel–Bulkley fluids, Journal of Petroleum Science and Engineering 60 (2) (2008) 105–124.

[30] K. Yasuda, Investigation of the analogies between viscometric and linear viscoelastic properties of polystyrene fluids, Ph.D. thesis, Massachusetts Institute of Technology (1979).

[31] M. M. Cross, Rheology of non-Newtonian fluids: a new flow equation for pseudoplastic systems, Journal of Colloid Science 20 (5) (1965) 417–437.

[32] D. M. Meter, R. B. Bird, Tube flow of non-newtonian polymer solutions: Part I. laminar flow and rheological models, AIChE Journal 10 (6) (1964) 878–881.

[33] R. Ellahi, A. Riaz, S. Nadeem, M. Ali, Peristaltic flow of carreau fluid in a rectangular duct through a porous medium, Mathematical problems in Engineering 2012.

[34] B. Gireesha, P. S. Kumar, B. Mahanthesh, S. Shehzad, A. Rauf, Nonlinear 3d flow of casson-carreau fluids with homogeneous–heterogeneous reactions: a comparative study, Results in physics 7 (2017) 2762–2770.

[35] F. Zami-Pierre, R. de Loubens, M. Quintard, Y. Davit, Effect of disorder in the pore-scale structure on the flow of shear-thinning fluids through porous media, Journal of Non-Newtonian Fluid Mechanics 261 (2018) 99–110.

[36] C. Airiau, A. Bottaro, Flow of shear-thinning fluids through porous media, Advances in Water Resources (2020) 103658.

[37] R. P. Chhabra, J. F. Richardson, Non-Newtonian Flow and Applied Rheology: Engineering Applications, Butterworth-Heinemann, 2011.

[38] M. Reddy, J. Reddy, Finite-element analysis of flows of non-Newtonian fluids in three-dimensional enclosures, International Journal of Nonlinear Mechanics 27 (1) (1992) 9–26.

[39] S. Fagbemi, P. Tahmasebi, M. Piri, Interaction between fluid and porous media with complex geometries: a direct pore-scale study, Water Resources Research 54 (9) (2018) 6336–6356.

[40] A. Khalifeh, J.-R. Clermont, Numerical simulations of non-isothermal three-dimensional flows in an extruder by a finite-volume method, Journal of Non-Newtonian Fluid Mechanics 126 (1) (2005) 7–22.

[41] H. Zhong, W. Zhang, H. Yin, H. Liu, Study on mechanism of viscoelastic polymer transient flow in porous media, Geofluids 2017.

[42] M. Tembely, A. AlSumaiti, M. Jouini, K. Rahimov, The effect of heat transfer and polymer concentration on non-newtonian fluid from pore-scale simulation of rock x-ray micro-ct, Polymers 9 (10) (2017) 509.

[43] H. Patel, J. Kuipers, E. Peters, Effect of flow and fluid properties on the mobility of multiphase flows through porous media, Chemical Engineering Science 193 (2019) 243–254.

[44] T. Clemens, K. Tsikouris, M. Buchgraber, L. M. Castanier, A. Kovscek, et al., Pore-scale evaluation of polymers displacing viscous oil–computational-fluid-dynamics simulation of micromodel ex-

periments, Spe Reservoir Evaluation & Engineering 16 (02) (2013) 144–154.

[45] O. Malaspinas, G. Courbebaisse, M. Deville, Simulation of generalized Newtonian fluids with the lattice Boltzmann method, International Journal of Modern Physics C 18 (12) (2007) 1939–1949.

[46] A. W. Liu, D. E. Bornside, R. C. Armstrong, R. A. Brown, Viscoelastic flow of polymer solutions around a periodic, linear array of cylinders: comparisons of predictions for microstructure and flow fields, Journal of Non-Newtonian Fluid Mechanics 77 (3) (1998) 153–190.

[47] D. Richter, G. Iaccarino, E. S. Shaqfeh, Simulations of three-dimensional viscoelastic flows past a circular cylinder at moderate reynolds numbers, Journal of fluid mechanics 651 (2010) 415.

[48] F. Alcocer, P. Singh, Permeability of periodic arrays of cylinders for viscoelastic flows, Physics of fluids 14 (7) (2002) 2578–2581.

[49] A. F. Morais, H. Seybold, H. J. Herrmann, J. S. Andrade Jr, Non-newtonian fluid flow through three-dimensional disordered porous media, Physical review letters 103 (19) (2009) 194502.

[50] S. De, J. Kuipers, E. Peters, J. Padding, Viscoelastic flow simulations in model porous media, Physical Review Fluids 2 (5) (2017) 053303.

[51] S. De, S. Das, J. Kuipers, E. Peters, J. Padding, A coupled finite volume immersed boundary method for simulating 3d viscoelastic flows in complex geometries, Journal of Non-Newtonian Fluid Mechanics 232 (2016) 67–76.

[52] P. de Anna, B. Quaife, G. Biros, R. Juanes, Prediction of the low-

velocity distribution from the pore structure in simple porous media, Physical Review Fluids 2 (12) (2017) 124103.

[53] F. J. Galindo-Rosales, L. Campo-Deaño, F. Pinho, E. Van Bokhorst, P. Hamersma, M. S. Oliveira, M. Alves, Microfluidic systems for the analysis of viscoelastic fluid flow phenomena in porous media, Microfluidics and nanofluidics 12 (1-4) (2012) 485–498.

[54] C. A. Browne, A. Shih, S. S. Datta, Pore-scale flow characterization of polymer solutions in microfluidic porous media, Small 16 (9) (2020) 1903944.

[55] E. M. Ekanem, S. Berg, S. De, A. Fadili, T. Bultreys, M. Rücker, J. Southwick, J. Crawshaw, P. F. Luckham, Signature of elastic turbulence of viscoelastic fluid flow in a single pore throat, Physical Review E 101 (4) (2020) 042605.

[56] S. De, P. Krishnan, J. Van Der Schaaf, J. Kuipers, E. Peters, J. Padding, Viscoelastic effects on residual oil distribution in flows through pillared microchannels, Journal of Colloid and Interface Science 510 (2018) 262–271.

[57] S. De, J. Van Der Schaaf, N. Deen, J. Kuipers, E. Peters, J. Padding, Lane change in flows through pillared microchannels, Physics of Fluids 29 (11) (2017) 113102.

[58] S. De, J. A. Kuipers, E. A. Peters, J. T. Padding, Viscoelastic flow past mono-and bidisperse random arrays of cylinders: flow resistance, topology and normal stress distribution, Soft Matter 13 (48) (2017) 9138–9146.

[59] C. A. Browne, A. Shih, S. S. Datta, Bistability in the unstable flow of

polymer solutions through pore constriction arrays, Journal of Fluid Mechanics 890.

[60] R. B. Bird, W. E. Stewart, E. N. Lightfoot, Transport Phenomena, John Wiley & Sons, 2007.

[61] N. P. Thien, R. I. Tanner, A new constitutive equation derived from network theory, Journal of Non-Newtonian Fluid Mechanics 2 (4) (1977) 353–365.

[62] P. J. Oliveira, F. T. Pinho, Analytical solution for fully developed channel and pipe flow of phan-thien–tanner fluids, Journal of Fluid Mechanics 387 (1999) 271–280.

[63] T. Shende, V. J. Niasar, M. Babaei, Effective viscosity and reynolds number of non-newtonian fluids using meter model, Rheologica Acta 60 (1) (2021) 11–21.

[64] F. Pimenta, M. Alves, Stabilization of an open-source finite-volume solver for viscoelastic fluid flows, Journal of Non-Newtonian Fluid Mechanics 239 (2017) 85–104.

[65] D. Cruz, F. Pinho, P. J. Oliveira, Analytical solutions for fully developed laminar flow of some viscoelastic liquids with a newtonian solvent contribution, Journal of non-newtonian fluid mechanics 132 (1-3) (2005) 28–35.

[66] T. J. Sadowski, R. B. Bird, Non-Newtonian Flow through Porous Media. I. Theoretical, Transactions of the Society of Rheology 9 (2) (1965) 243–250.

[67] B. Ghanbarian, A. G. Hunt, R. P. Ewing, M. Sahimi, Tortuosity in

porous media: a critical review, Soil Science Society of America Journal 77 (5) (2013) 1461–1477.

[68] S. Li, M. Dong, P. Luo, A crossflow model for an interacting capillary bundle: Development and application for waterflooding in tight oil reservoirs, Chemical Engineering Science 164 (2017) 133–147.

[69] M. M. Błaszczyk, J. P. Sek, Ł. Przybysz, Capillary bundle model for gravitational flow of emulsion through granular media and experimental validation, Chemical Engineering Science 155 (2016) 415–427.

[70] P. P. Jagdale, D. Li, X. Shao, J. B. Bostwick, X. Xuan, Fluid rheological effects on the flow of polymer solutions in a contraction–expansion microchannel, Micromachines 11 (3) (2020) 278.

[71] H. Park, M. Hawley, R. Blanks, The flow of non-newtonian solutions through packed beds, Polymer Engineering & Science 15 (11) (1975) 761–773.

[72] H. Jasak, A. Jemcov, Z. Tukovic, et al., OpenFOAM: A C++ library for complex physics simulations, in: International workshop on coupled methods in numerical dynamics, Vol. 1000, IUC Dubrovnik Croatia, 2007, pp. 1–20.

[73] F. Moukalled, L. Mangani, M. Darwish, et al., The finite volume method in computational fluid dynamics, Vol. 6, Springer, 2016.

[74] S. V. Patankar, D. B. Spalding, A calculation procedure for heat, mass and momentum transfer in three-dimensional parabolic flows, in: Numerical prediction of flow, heat transfer, turbulence and combustion, Elsevier, 1983, pp. 54–73.

[75] R. I. Issa, Solution of the implicitly discretised fluid flow equations by operator-splitting, Journal of computational physics 62 (1) (1986) 40–65.

[76] J. H. Ferziger, M. Perić, R. L. Street, Computational methods for fluid dynamics, Vol. 3, Springer, 2002.

[77] F. Pimenta, M. Alves, rheotool, https://github.com/fppimenta/rheoTool (2016).

[78] M. Alves, P. Oliveira, F. Pinho, A convergent and universally bounded interpolation scheme for the treatment of advection, International journal for numerical methods in fluids 41 (1) (2003) 47–75.

[79] A. H. Kohanpur, M. Rahromostaqim, A. J. Valocchi, M. Sahimi, Two-phase flow of CO2-brine in a heterogeneous sandstone: Characterization of the rock and comparison of the lattice-boltzmann, pore-network, and direct numerical simulation methods, Advances in Water Resources 135 (2020) 103469.

[80] J. Schindelin, I. Arganda-Carreras, E. Frise, V. Kaynig, M. Longair, T. Pietzsch, S. Preibisch, C. Rueden, S. Saalfeld, B. Schmid, et al., Fiji: an open-source platform for biological-image analysis, Nature methods 9 (7) (2012) 676–682.

[81] M. Prodanovic, M. Esteva, M. Hanlon, G. Nanda, P. Agarwal, Digital rocks portal: a repository for porous media images. 10.17612 (2015).

[82] A. Rabbani, S. Salehi, Dynamic modeling of the formation damage and mud cake deposition using filtration theories coupled with sem image processing, Journal of Natural Gas Science and Engineering 42 (2017) 157–168.

[83] X. Chen, H. Marschall, M. Schäfer, D. Bothe, A comparison of stabilisation approaches for finite-volume simulation of viscoelastic fluid flow, International Journal of Computational Fluid Dynamics 27 (6-7) (2013) 229–250.

[84] M. Escudier, R. Poole, F. Presti, C. Dales, C. Nouar, C. Desaubry, L. Graham, L. Pullum, Observations of asymmetrical flow behaviour in transitional pipe flow of yield-stress and other shear-thinning liquids, Journal of Non-Newtonian Fluid Mechanics 127 (2-3) (2005) 143–155.

[85] S. Liu, Y. Zhang, W. Xing, W. Jian, Z. Liu, T. Li, Y. Song, Laboratory experiment of co2–ch4 displacement and dispersion in sandpacks in enhanced gas recovery, Journal of Natural Gas Science and Engineering 26 (2015) 1585–1594.

[86] A. Rodríguez de Castro, G. Radilla, Non-Darcian flow experiments of shear-thinning fluids through rough-walled rock fractures, Water Resources Research 52 (11) (2016) 9020–9035.

[87] P. Mohammadmoradi, A. Kantzas, Pore scale investigation of wettability effect on waterflood performance, in: SPE Annual Technical Conference and Exhibition, Society of Petroleum Engineers, 2016.

[88] U. Eberhard, H. Seybold, E. Secchi, J. Jiménez-Martínez, P. Rühs, A. Ofner, J. Andrade, M. Holzner, Mapping the local viscosity of non-newtonian fluids flowing through disordered porous structures, Scientific Reports 10 (1) (2020) 1–12.